ANALYSIS OF THE RESULTS FOR TC3-1 PRESENTED BY ONERA AND INSTITUTE OF MECHANICS MSU

V.Gromov*, V. Sakharov* and O.Rousaund**

*Institute of Mechanics Moscow State University, 1 Michurinskii Pr., 119192 Moscow, Russia,
gromov@imec.msu.ru   sakharov@imec.msu.ru

** ONERA, Department Modeling of Aerodynamics and Energetics, 2 Avenue Edouard Belin, 31055 Toulouse, France, rouzaud@onecert.fr

Проведен сравнительный анализ полей течений, конвективных и радиационных тепловых потоков к поверхности модели Марсианского спускаемого аппарата, полученных в расчетах обтекания на различных сетках для условий TC3-1. Подтверждена, обнаруженная ранее сложная топология течения с образованием нескольких отрывных зон на подветренной стороне модели с использованием одноблочной и нескольких многоблочных расчетных сеток. Конвективные тепловые потоки вдоль поверхности модели, полученные в расчетах для всех типов сеток, совпадают с высокой точностью. Радиационные тепловые потоки в LTE приближении на наветренной и подветренной сторонах модели также хорошо согласуются друг с другом для всех вариантов расчетов и использованных радиационных моделей.

1. INTRODUCTION

The results of the mandatory case TC3-1 computations performed under the INTAS Project No.5204 (Task 5.1) involving flow field (NIIMech, ONERA) and radiation (NIIMech and ONERA) computations are presented and analyzed. NIIMech has performed the flow and RHT computations by over the whole body using the mono-domain grid G-OB-TC3-1, the multi-block grid G-MB-TC3-1 and a multi-block grid developed in NIIMech. Computations have also been performed by NIIMech using the mono-domain grid G-FS-TC3-1 but only over the front shield. The grids G-OB-TC3-1, G-MB-TC3-1 and G-FS-TC3-1 were taken from Workshop's 2003 site. ONERA has presented its flow and RHT computations on the grid G-OB-TC3-1. All contributions are gathered in Table 1.

GRID/TEAM	NIIMech	ONERA
G-OB-TC3-1	Flow + RHT	Flow + RHT
G-FS-TC3-1	Flow + RHT	Flow
G-MB-TC3-1	Flow + RHT	
NIIM grid	Flow + RHT	
CFD solver	HIGHTEMP	CELHYO2D
RHT solver + Optical model	HIGHTEMP + ABSORB_AGM (IPM)	ASTRE + EM2C model

Table1. Contributions to TC3

Simultaneously comparisons with results included in synthesis [2] will be discussed.

2. MANDATORY TEST-CASE TC3-1 DEFINITION
2.1. Geometry
An axially symmetric vehicle is defined based on a sphere-cone assembly with a cylindrical after body. The shape and dimensions (in cm) of this vehicle are presented in Fig.1.
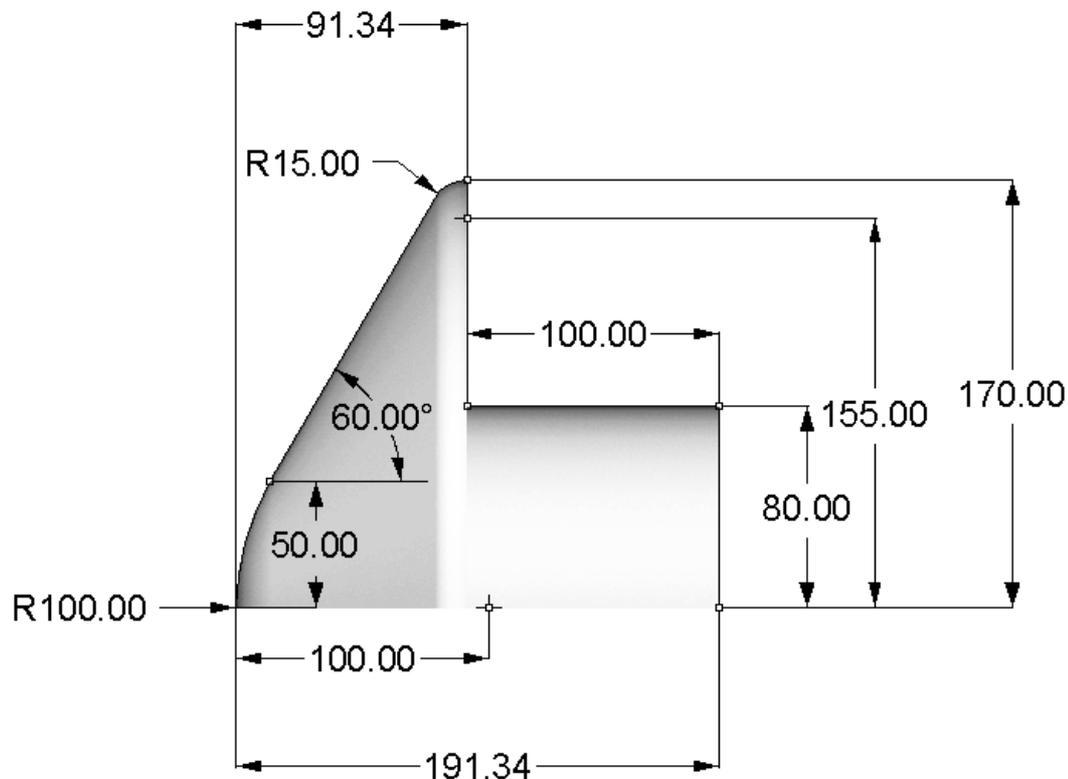

Fig.1: Shape of the axially-symmetric derived model (dimensions in cm)

2.2. Martian atmosphere composition model
The Martian atmosphere is assumed to have pure CO_2 (atmosphere model ATM-SPECIES-1)

2.3. Flight trajectory condition
Density – 2.933 10^{-4} kg/m^3;
Velocity – 5223 m/s;
Temperature – 140 K

2.4. Gas-phase model
2.4.1. Chemical modeling
The 5-species (O, C, O_2, CO, CO_2) modified Park'94 chemistry model used for this mandatory test case is given hereafter. Following Arrhenius reaction constant rates, it writes as:

$$\text{Forward reaction rates } K_f(T) = A_f T^{b_f} \exp(-E_f / T)$$

and

$$\text{Reverse reaction rates } K_r(T) = A_r T^{b_r} \exp(-E_r / T)$$

18 reactions are displayed and the reaction rate constants are given next:

		K_f $(m^3.mol^{-1}.s^{-1})$			K_r $(m^3.mol^{-1}.s^{-1}$ or $m^6.mol^{-1}.s^{-1})$		
		A_f	b_f	E_f	A_r	b_r	E_r
1) $CO2 + O2$	$= CO + O + O2$	6.90e15	-1.5	63275	1.14e05	-0.75	535.
2) $CO2 + O$	$= CO + O + O$	1.38e16	-1.5	63275	2.28e05	-0.75	535.
3) $CO2 + C$	$= CO + O + C$	1.38e16	-1.5	63275	2.28e05	-0.75	535.
4) $CO2 + CO$	$= CO + CO + O$	6.90e15	-1.5	63275	1.14e05	-0.75	535.
5) $CO2 + CO2$	$= CO + O + CO2$	6.90e15	-1.5	63275	1.14e05	-0.75	535.
6) $CO + O2$	$= C + O + O2$	2.30e14	-1.0	129000	5.13e06	-1.0	0.
7) $CO + O$	$= C + O + O$	3.40e14	-1.0	129000	7.59e06	-1.0	0.
8) $CO + C$	$= C + O + C$	3.40e14	-1.0	129000	7.59e06	-1.0	0.0
9) $CO + CO$	$= C + O + CO$	2.30e14	-1.0	129000	5.13e06	-1.0	0.0
10) $CO + CO2$	$= C + O + CO2.$	2.300e14	-1.0	129000	5.13e06	-1.0	0.0
11) $O2 + C$	$= O + O + C$	1.00e16	-1.5	59500	1.0e07	-1.0	0.0
12) $O2 + CO$	$= O + O + CO$	2.00e15	-1.5	59500	2.0e06	-1.0	0.0
13) $O2 + CO2$	$= O + O + CO2$	2.00e15	-1.5	59500	2.0e06	-1.0	0.0
14) $CO + CO$	$= CO2 + C$	2.33e03	0.5	65710	4.6e06	-0.25	0.0
15) $CO + O$	$= O2 + C$	3.90e07	-0.18	69200	1.34e08	-0.43	0.0
16) $CO2 + O$	$= O2 + CO$	2.10e07	0.0	27800	4.11e04	0.5	23800
17) $O2 + O2$	$= O + O + O2$	2.00e15	-1.5	59500	2.0e06	-1.0	0.0
18) $O2 + O$	$= O + O + O$	1.00e16	-1.5	59500	1.0e07	-1.0	0.0

2.4.2. Thermodynamics

Rigid rotator – harmonic oscillator model is used for the molecules thermodynamic functions calculations. Characteristic vibrational (T_V) and rotational (T_R) temperatures are given in the following table

Species	T_V ,K	T_R ,K
CO_2	1890, 954(2), 3360	0.56
CO	3121	2.78
O_2	2270	2.08

The enthalpy formations are provided in the next table:

Species	H_0^f (J/kg)
CO_2	-8.94368e6
CO	0.
O_2	-3.9475e6
C	5.97225e7
O	1.54057e7

2.4.3. Transport properties

The mixture law of Armaly&Sutton is used for mixture viscosity computation

$$\mu_{mixture} = \sum_{s=1}^{ns} \frac{\mu_s}{1 + \sum_{\substack{k=1 \\ k \neq s}}^{ns} \frac{X_k}{X_s} \left(F_{sk} + \sqrt{\frac{\mu_s}{\mu_k}} \left(\frac{\hat{M}_k}{\hat{M}_s} \right)^{1/4} B_{sk} \right)^2 \left(\frac{\hat{M}_s}{\hat{M}_s + \hat{M}_k} \right) \left(\frac{5}{3A_{sk}^*} + \frac{\hat{M}_k}{\hat{M}_s} \right) / \sqrt{8 \left(1 + \frac{\hat{M}_s}{\hat{M}_k} \right)}}$$

where $A_{sk} = 1.25$, $B_{sk} = 0.78$, $F_{sk} = 1$.

Blottner correlation formulas is used for pure gas viscosity computation:

$$\mu_s = 0.1\exp\left[\left(A_s^\mu \ln T + B_s^\mu\right)\ln T + C_s^\mu\right]$$

where $A_s^\mu, B_s^\mu,$ et C_s^μ are given on following table :

Species	A_s^μ	B_s^μ	C_s^μ
O2	0.0449290	-0.0826158	-9.2019475
CO	-0.014044	0.887198	-13.269815
CO2	-0.026654	1.107305	-14.291274
O	0.0436378	-0.0335511	-9.5767430
C	-0.007140	0.768602	-12.956246

Thermal conductivity is defined according to a constant Prandtl number for the whole computational domain

$$\Pr = \frac{\mu_{mix}C_p}{\lambda_{mix}} = 0.66$$

The Fick law is used to calculate mass diffusion rate of species *s:*

$$\vec{J}_s = -\rho D \frac{\partial c_s}{\partial \vec{r}}$$

Constant Lewis number is assumed throughout the flow field as:

$$Le = \frac{\rho D C_p}{\lambda_{mix}} = 1$$

2.5. Gas-wall interaction model
The surface of the vehicle is fully neutral for all chemical processes.
The surface is an isothermal with T_{w-FHS} =1500K for the heat shield facing the flow and

T_{w-AFT} =500 K for the rest of the vehicle.

3. CFD AND RHT COMPUTATIONS
3.1. Grids
Navier-Stokes and radiation calculations have been performed using four different grids adapted to body surface. The multi-domain NIIMech grid involves 8 blocks with total 37740 cells number (Fig. 2). The grid is adapted to bow shock during computations so that the some specified grid line is placed into the bow shock region during of the N-S integration. At this line the ρ/ρ_∞ is given (about 4-5).
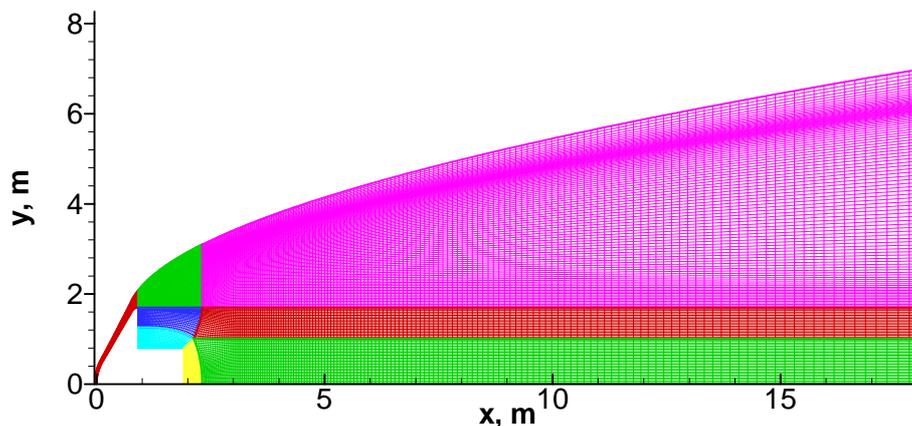

Fig.2. NIIMech multi-domain grid

The mandatory multi-domain grid G-MB-TC3-1 (R-Tech) involves 29 blocks with 24336 cells number is presented in Fig.3. The grid has a larger extension in the rear section compared with the multi-domain NIIMech grid.
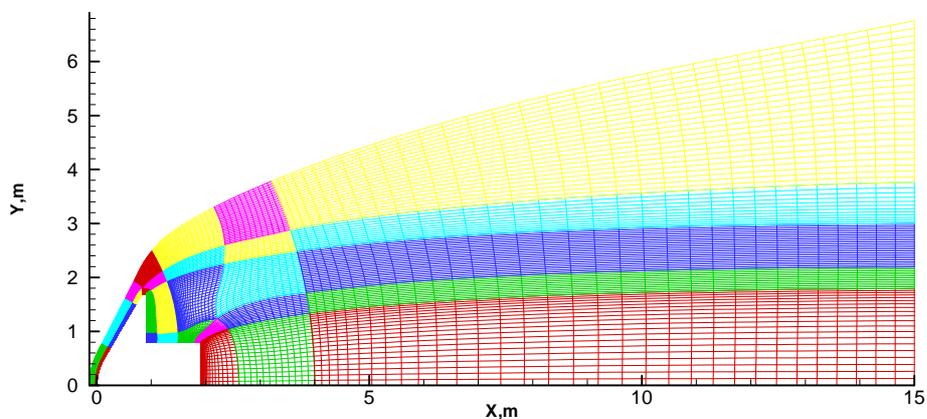

Fig.3: Multi-domain grid G-MB-TC3-1

The mandatory mono-domain grid G-OB-TC3-1 (ONERA) with 192x100 cells number is displayed in Fig.4. The grid is refined near the expected shock location.
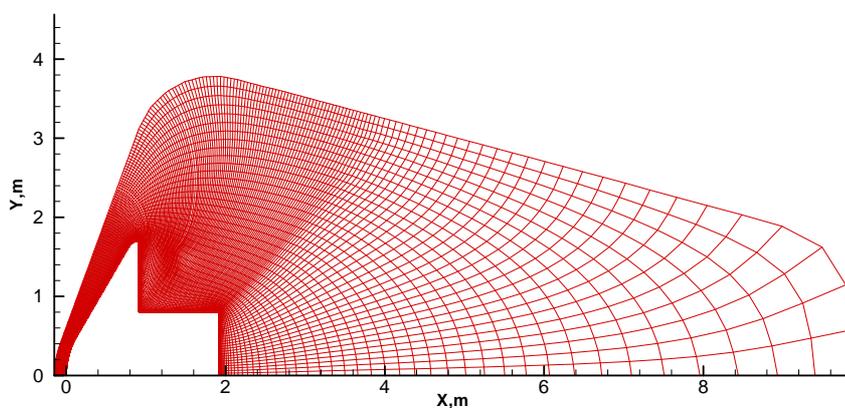

Fig.4: Mono-domain grid G-OB-TC3-1

The mandatory mono-domain grid G-FS-TC3-1 for the fore-body region with 24x86 cells number is displayed in Fig.5.
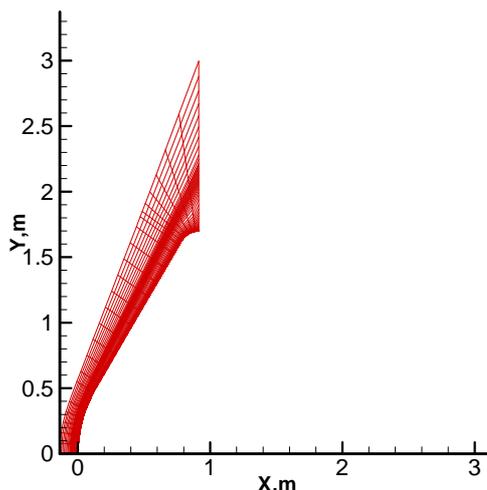
Fig.5: Mono-domain grid G-FS-TC3-1

3.2. NIIMech's Navier-Stokes solver.

NIIMech calculations have been performed using Computer System HIGHTEMP [3]. The HIGHTEMP technique is based on a package of Navier-Stokes (NS) solvers integrated with databases on transport, thermodynamics and thermo-chemical properties of individual species and service codes. The NS solvers are realized for the mostly-used classes of high temperature thermo-chemical gas-phase models from perfect gas to multi-temperature and multi-species ionized gas mediums. Nonequilibrium chemical reactions, ionization, relaxation of internal energy modes can be included in kinetic model and their coupling can be accounted for. Gas-phase models can be used with various gas-wall interaction models. Slip effects, finite rate energy exchanges, surface catalysis and ablation can be taken into account in the formulation of the boundary conditions.

The NS equations are solved on multi-block structured meshes through a finite volume approach. With this approach, the finite difference equations system consists of numerical analogs of the conservation equations for the quadrilateral cells covering the computational domain and the difference approximation of the boundary conditions. This method yields an approximate solution at the center of each cell and at the center of each cell side lying on the wall. The inviscid fluxes across cell faces are calculated from result of the exact Riemann problem solution. The Riemann problem is solved for the frozen state of all considerate non-equilibrium processes. The interfacial values are defined by the limited one-dimensional extrapolation of primitive variables from the cell-centers to the cell faces. The numerical viscous fluxes across cell faces are evaluated using the central and one-sided difference formulas of second order accuracy. Steady-state solution is obtained through an implicit iterative procedure. At each iteration the flow field parameters are computed by Gauss-Seidel line relaxation numerical method.

3.3. NIIMech's 2D RHT solver

Radiation heat transfer in cylindrical coordinates (x, y, ψ) is described by balance equation written for control domain S with boundary δS in the meridian plane $(x, y, 0)$

$$\int_{\delta S} \vec{n} \cdot \vec{\Omega} I_\omega y \, ds = \int_S \kappa_\omega (\bar{I}_\omega - I_\omega) y \, dS + \sin \theta \int_S \left(\cos \varphi I_\omega + \sin \varphi \, \partial I_\omega / \partial \varphi \right) dS;$$

6

where $I_\omega\left(x,y,\vec{\Omega}\right)$ and $\overline{I}_\omega(x,y)$ are the spectral intensity of the medium and blackbody radiation, κ_ω is the spectral absorption coefficient, $\vec{n}=(n_x,n_y)$ is an unit outward normal to δS, $\vec{\Omega}$ is a direction of energy passing defined as:

$$\vec{\Omega}(\theta,\varphi)=(\cos\theta,\sin\theta\cos\varphi),$$

where θ is the polar angle between x axes and $\vec{\Omega}$, φ is the azimuthal angle.

The finite volume approach is used to solve *RHT* equations also. Spectral intensity $I_\omega\left(x,y,\vec{\Omega}\right)$ is considered as constant for some discrete intervals of spectra and $\vec{\Omega}$. Difference finite volume equations for discrete values of I_ω (denoted as $I^{\mathbf{n}}$) are written in form of the numerical energy balance for cells (i,j)

$$f_{i+1/2,j}^{\mathbf{n}}-f_{i-1/2,j}^{\mathbf{n}}+f_{i,j+1/2}^{\mathbf{n}}-f_{i,j-1/2}^{\mathbf{n}}+\kappa_{i,j}^{k}\left[I_{i,j}^{\mathbf{n}}-\overline{I}_{i,j}^{k}\right]y_{i,j}S_{i,j}$$

$$-\sin\theta_m\left[\cos\varphi_n I_{i,j}^{\mathbf{n}}+\sin\varphi_n\frac{\Delta_\varphi I_{i,j}^{\mathbf{n}}}{\Delta\varphi}\right]S_{i,j}=0;$$

$$\mathbf{n}=(k,m,n),\quad k=1,...,K;\quad m=1,...,2M;\quad n=0,...,N;$$

$$I^{\mathbf{n}}=I_{\omega_k}\left(\vec{\Omega}_{m,n}\right),\quad \vec{\Omega}_{m,n}=(\cos\theta_m,\sin\theta_m\cos\varphi_n);\quad \overline{I}^k=\overline{I}_{\omega_k}$$

$$\omega_k=\omega_S+(k+0.5)\Delta\omega,\quad \Delta\omega=(\omega_F-\omega_S)/K$$

$$\kappa^k=\frac{1}{L}\sum_{l=1}^{L}\kappa_{\omega_k^l},\quad \omega_k^l=\omega_S+(k-1)\Delta\omega+(l-0.5)\Delta\omega/L,\quad l=1,...,L$$

$$\sin\theta_m=1/(M\Delta_m\theta),\quad \Delta_m\theta=\arccos(1.-m/M)-\arccos(1.-(m-1)/M),$$

$$\cos\theta_m=1.-(m-0.5)/M,\quad \varphi_n=n\Delta\varphi,\quad \Delta\varphi=\pi/N$$

Here *k, m, n* are numbers of intervals of spectra and angles θ, φ accordingly; *l* is number of the spectral point on interval $\Delta\omega$; $f_{i\pm1/2,j}^{\mathbf{n}}$, $f_{i,j\pm1/2}^{\mathbf{n}}$ are fluxes of $I^{\mathbf{n}}$ across corresponding cell faces; $\Delta_\varphi I_{i,j}^{\mathbf{n}}=I_{i,j}^{(k,m,n+1)}-I_{i,j}^{(k,m,n)}$.

Radiation fluxes across the cell side are calculated using known "upwind" approximation. For example

$$f_{i+1/2,j}^{\mathbf{n}}=(\vec{s}_{i+1/2,j}\vec{\Omega}_{m,n})y_{i+1/2,j}I_{i+1/2,j}^{\mathbf{n}},$$

$$I_{i+1/2,j}^{\mathbf{n}}=\begin{cases}I_{i,j}^{\mathbf{n}} & for\ (\vec{n}_{i+1/2,j}\vec{\Omega}_{m,n})\geq 0\\ I_{i+1,j}^{\mathbf{n}} & for\ (\vec{n}_{i+1/2,j}\vec{\Omega}_{m,n})<0\end{cases},$$

$\vec{s}_{i+1/2,j}$ is a vectorial length of the cell side.

For every set $\mathbf{n}=(k,m,n)$ solution of numerical *RHT* equations is performed by the several walks of cells in different sequence starting from the boundaries. Wall radiation heat flux is defined by summation of the spectral radiation heat flux to the surface body over all wave number and angle intervals

$$q_{w,i}^{rad}=-\frac{2\Delta\varphi\Delta\omega}{M}\sum_{k=1}^{K}\sum_{m=1}^{2M}\sum_{n=0}^{N}r_n I_{i,1}^{(k,m,n)}\left(\vec{n}_{i,1/2}\cdot\vec{\Omega}_{m,n}\right),\quad \left(\vec{n}_{i,1/2}\cdot\vec{\Omega}_{m,n}\right)<0$$

$$r_0=r_N=0.5;\quad r_n=1,\quad n=1,...,N\text{-}1$$

The multigroup LTE model taking into account the CO_2 emission induced by vibrational-rotational transitions in wave number interval 10^3- $5*10^3$ cm^{-1} (IR) was used for calculations. The ABSORB_AGM code developed by IPM [4] team was employed for computations of the spectral

adsorption coefficients. For calculations of CO and CO_2 adsorption coefficients in IR spectral region this code uses tabular data presented in Ref. 5. For NIIMech RHT calculations number of spectral groups K=100, number of spectral points in the group L=10, numbers of the direction intervals 2M=20, N=20.

4. FLOW COMPUTATIONS RESULTS
4.1. Front shield
4.1.1. Stagnation line
Distributions of some flow parameters along forward stagnation line predicted by ONERA and NIIMech calculations are illustrated in Figs. 7–8.
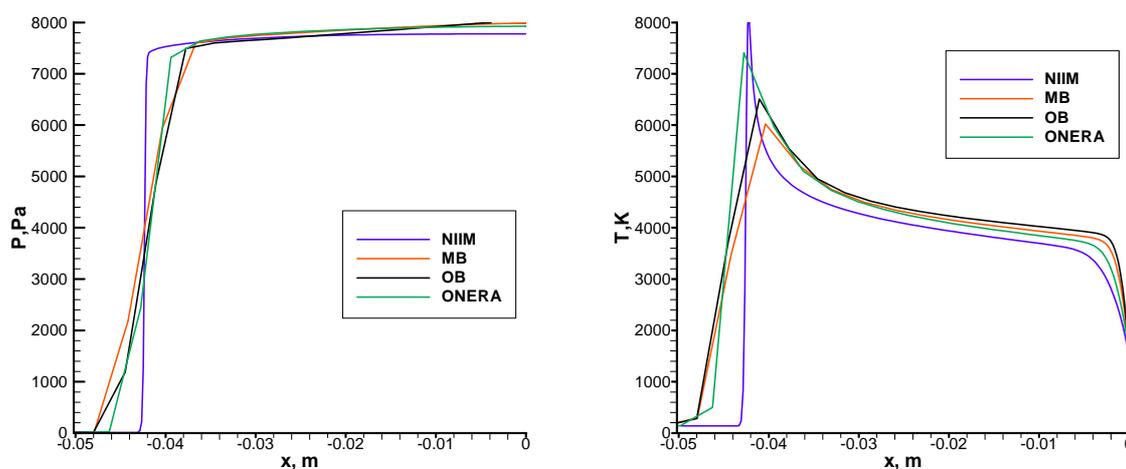
Fig 7: Static pressure and temperature along stagnation line

   As seen the pressure and temperatures profiles computed by NIIMech on the G-OB-TC3-1 grid and on the G-MB-TC3-1 grids are close together. The ONERA (G-OB-TC3-1 grid) maximum temperature is 1000 K higher compared with NIIMech's result on the same grid. The NIIMech multi-domain grid adapted to bow shock gives the highest temperature (2000 K difference in temperature maxima compared with G-OB-TC3-1 and G-MB-TC3-1 grids) and difference in shock positioning. The NIIMech multi-domain grid is meant to capture the bow shock much more precisely than the others ones. The static pressure predicted by the ONERA and NIIMech are closest. Some differences are observed compared with NIIMech calculations on the G-MB-TC3-1 grid. The G-MB-TC3-1 grid is not refined in the longitudinal direction in the shock wave region. From the comparisons with [2], it can be concluded that NIIMech adapted grid is better for capture shock and therefore the temperature peak is the highest compared with other contributions.
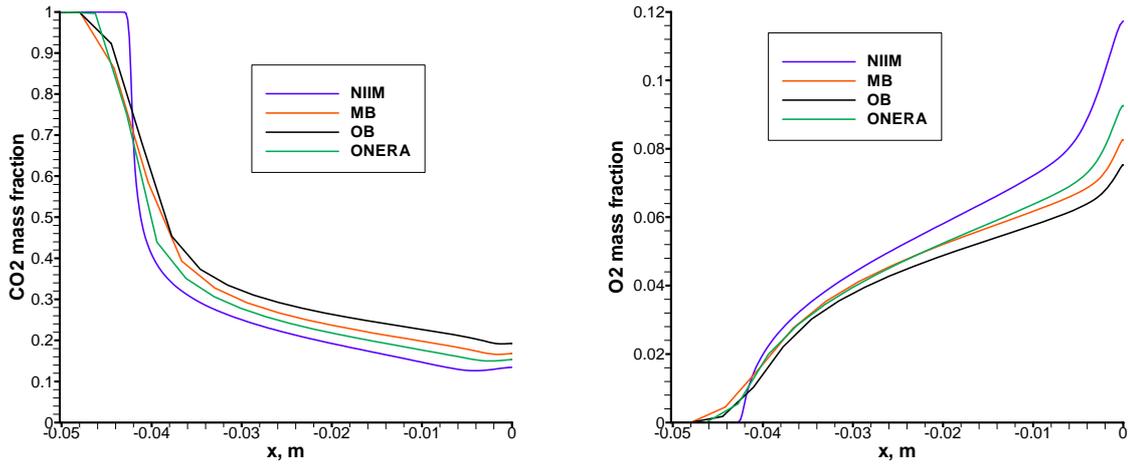
Fig 8: CO_2 & O_2 mass fractions along stagnation line

Regarding the species profiles along the stagnation line the results of ONERA on the G-MB-TC3-1 grid and NIIMech's results on the adapted grid are closer; but the effect of the grid refinement near the shock leads to lower values of CO_2 at the wall and inversely for the O_2 (Fig.8). The NIIMech's CO_2 and O_2 profiles obtained on the adapted grid are most close to the same ones obtained on the RTech ref. mono-domain and ONERA ref. mono-domain grids [2].

4.1.2. Front shield wall

The wall pressure on the front shield is shown on Fig. 9 for all grids computed by NIIMech and the monoblock grid computed by ONERA. All results are comparable and in a good agreement with results given in [2]. The main differences are observed on the conical part and maximum discrepancy between all is 100 Pa, i.e. 1.5%.
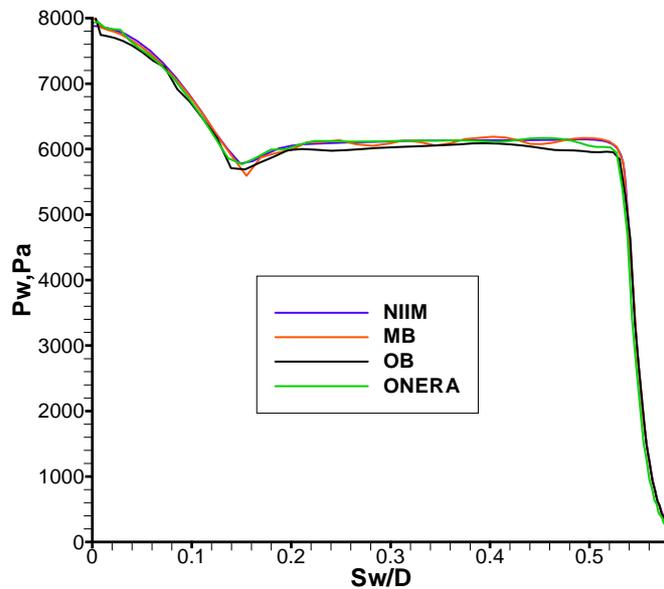
Fig. 9: Wall pressure P_w on the front shield
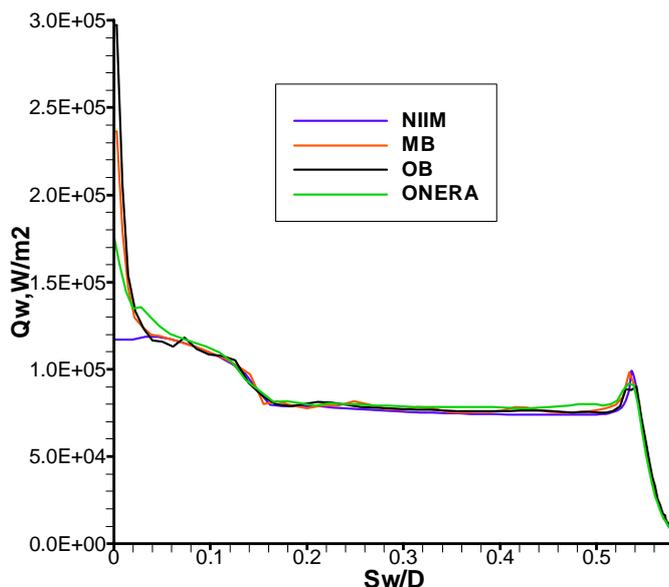
Fig. 10: Wall heat flux Q_W on the front shield

Fig. 10 shows the wall heat flux distributions on the various grids used. All results are close on the conical part but the discrepancies between the different computations are much larger than for pressure. Differences on the conical part are less than 5%. The main differences are observed in the stagnation point region. The adapted NIIMech grid give result without non-physical maximum connected with well known non-adapted grid problems. It was connected with coincidence between grid lines and shock wave region. The heat peak at the shoulder is resolved equally well for all calculations.
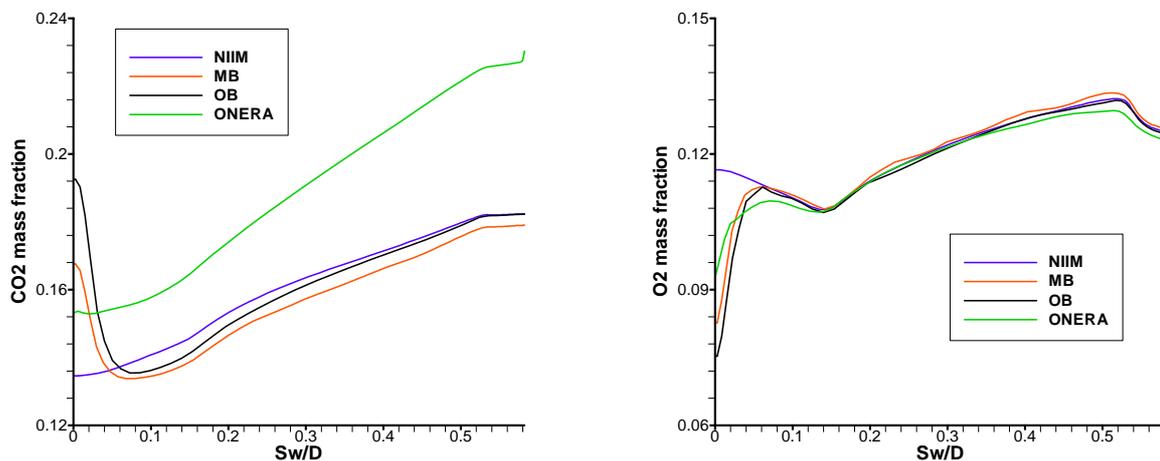
Fig. 11: Wall CO_2 and O_2 mass fractions on the front shield

Fig. 11 shows the CO_2 & O_2 mass fraction distributions along the front shield surface. The main differences in CO_2 distributions are clearly seen not only at stagnation point associated to previously mentioned grid problem but also between NIIMech and ONERA computations at the conical part (about 16% - 20%)using the same grid.

After-body

4.2.1. <u>Wall data</u>

The comparisons of the wall pressure and the heat flux distributions on the vehicle after-body are illustrated on Fig. 12 for all the calculations.
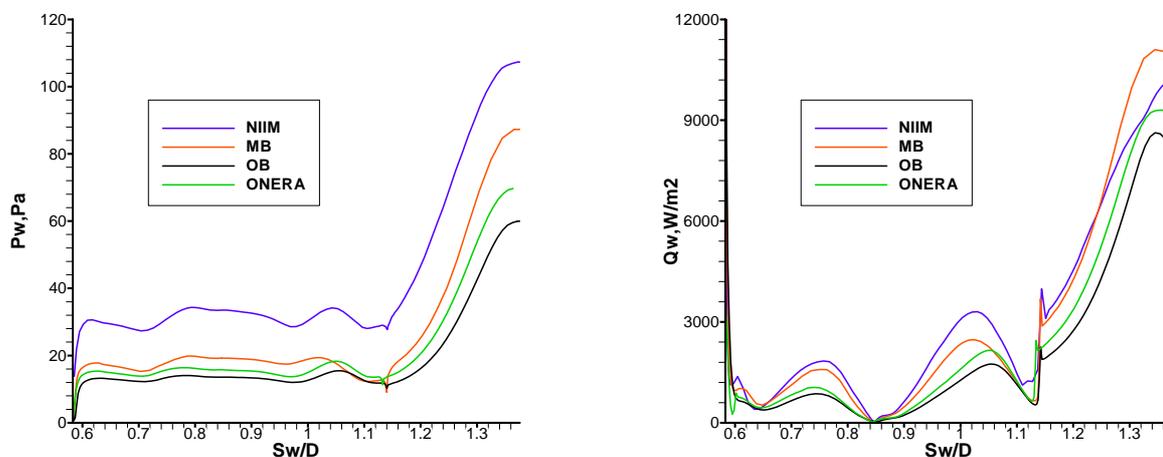

Fig. 12: Wall pressure and convective heat flux on the after-body

ONERA and NIIMech's predicted pressure distributions are in good agreement except for the NIIMech grid. The NIIMech adapted multi-domain grid gives an offset in pressure compared to the other solutions. NIMMech's result is very close to the pressure distribution obtained on R-Tech adapted multi-domain grids [2]. Conversely to [2] the heat flux distributions are different for all the cases. Quite small discrepancies in the heat flux peaks are observed for ONERA and NIIMech results for the same mono-domain grid. Regarding the heat flux distributions for G-MB-TC3-1 and NIIMech multi-domain adapted grids, these distributions are closest at the back cylindrical surface but there are differences in the back stagnation point.

The CO_2 & O_2 mass fractions on the after-body are displayed in Fig. 13. The maximal discrepancy in chemical composition is observed between ONERA and NIIMech calculations obtained on the same G-OB-TC3-1 grid.
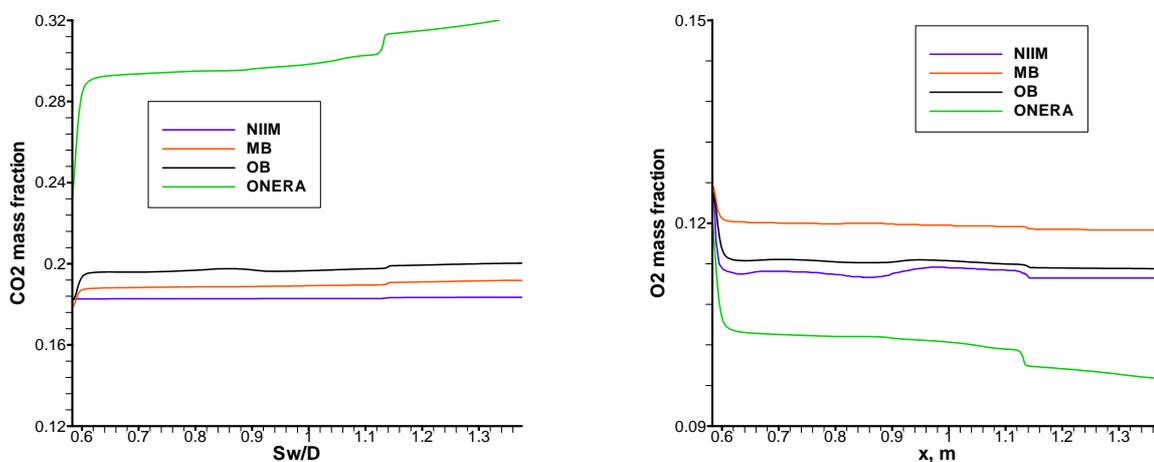

Fig. 13: Wall mass fractions CO_2 & O_2 on the after-body

4.2.2. Flow field data

The extensive analysis of impact of grid topology on the wake flow was carried out in [2]. The comparison the flow field topology on G-OB-TC3-1 grid by ONERA (Fig. 14) and by NIIMech (Fig. 15) is presented.   On these figures the longitudinal velocity component contour are shown also.
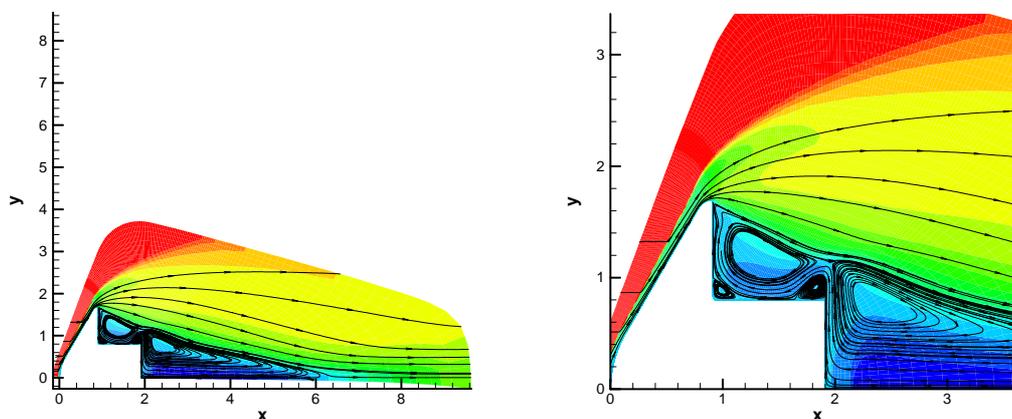

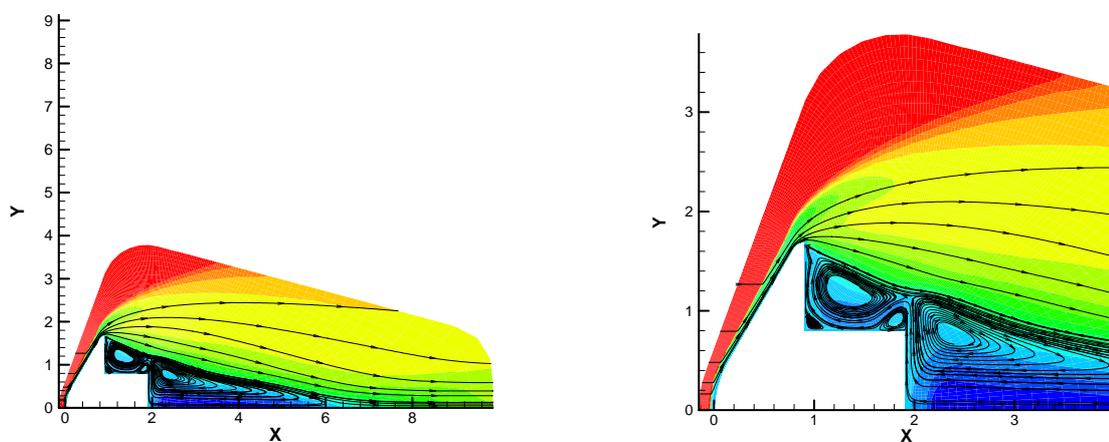Fig. 14: Flow topology in the wake: ONERA computation on grid G-OB-TC3-1

Fig. 15: Flow topology in the wake: NIIMech computation on grid G-OB-TC3-1

Both computations seem practically identical. The wake closure point is located between 6 and 6.5 m. There are four observed vortices: three along the cylindrical part and one trailing vortex.

Computation performed on multi-domain NIIMech grid adapted to the bow shock shows the appearance of an additional fifth vortex behind the shield near the shoulder (Fig. 16).
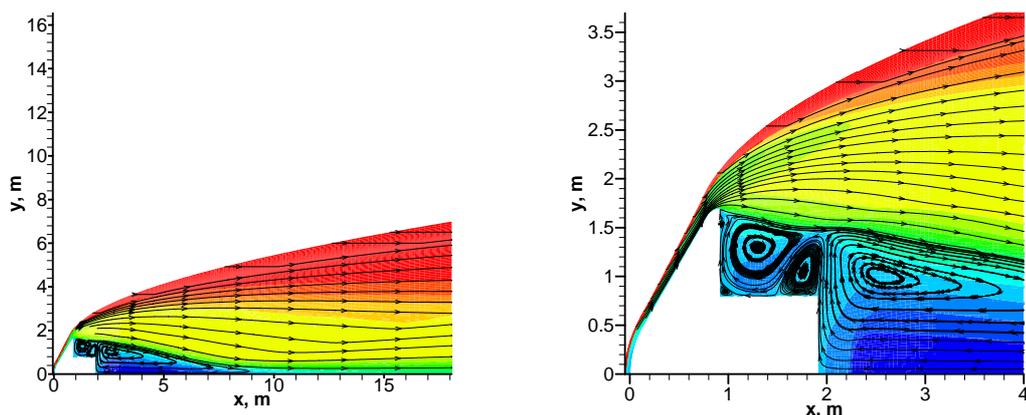
Fig. 16: Flow topology in the wake: computation on NIIMech grid

In comparison with calculations on G-OB-TC3-1 grid, the wake closure point is located at a distance between 9 and 10 m.
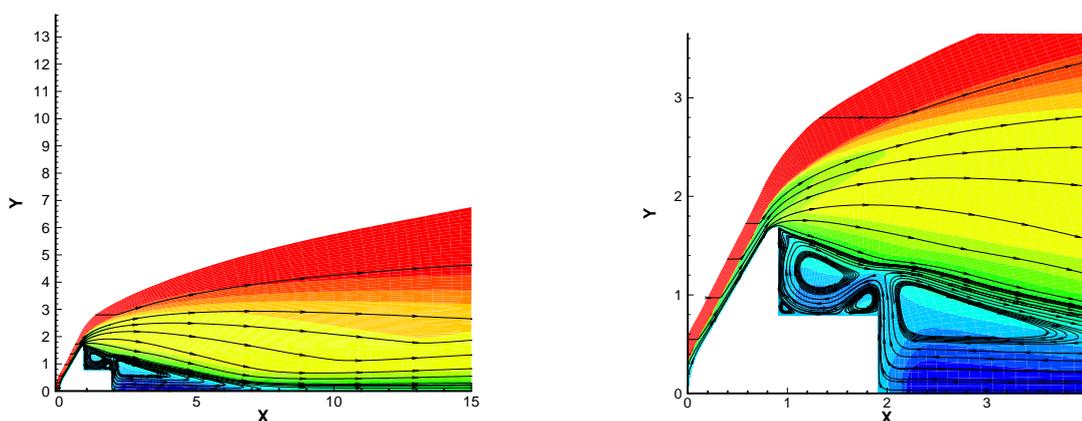

Fig. 17: Flow topology in the wake: NIIMech computation on G-MB-TC3-1 grid

In comparison with calculations on the G-OB-TC3-1 and NIIMech grids, the wake closure point on the G-MB-TC3-1 grid is located at distance between 7 and 8 (Fig. 17). There are five observed vortices as well as on the NIIMech grid.

All calculations have been developed by NIIMech and ONERA gave flow topology just not like as calculations are presented in [2] where calculation only on the adapted multi-domain R-Tech grid led to appearance of third vortex.

4.2.3. <u>Symmetry axis data</u>
The axial wake parameters in Fig. 18 are in line with flow field topology discussed above. The pressure and temperature maxima correspond to the location of the wake closure points. The best qualitative agreement from [2] is observed for R-Tech ref. mono-domain and ONERA ref. mono-domain grids.
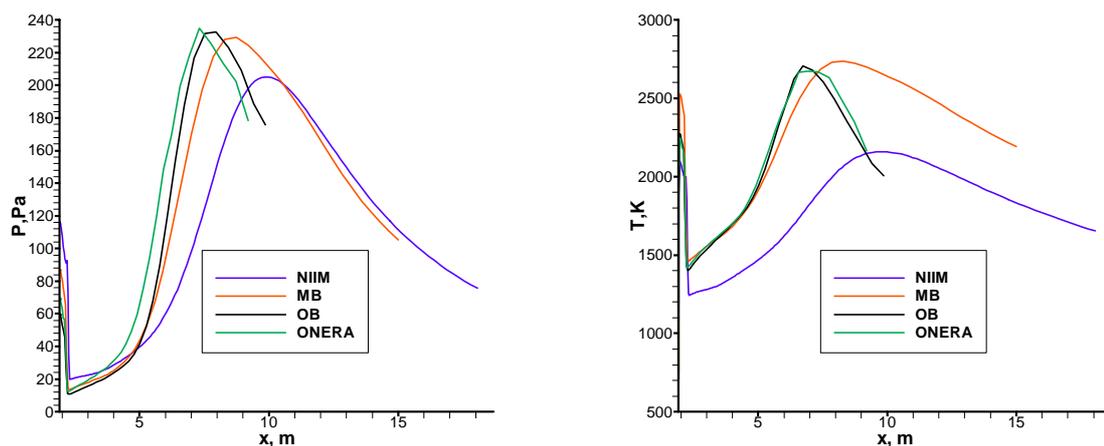
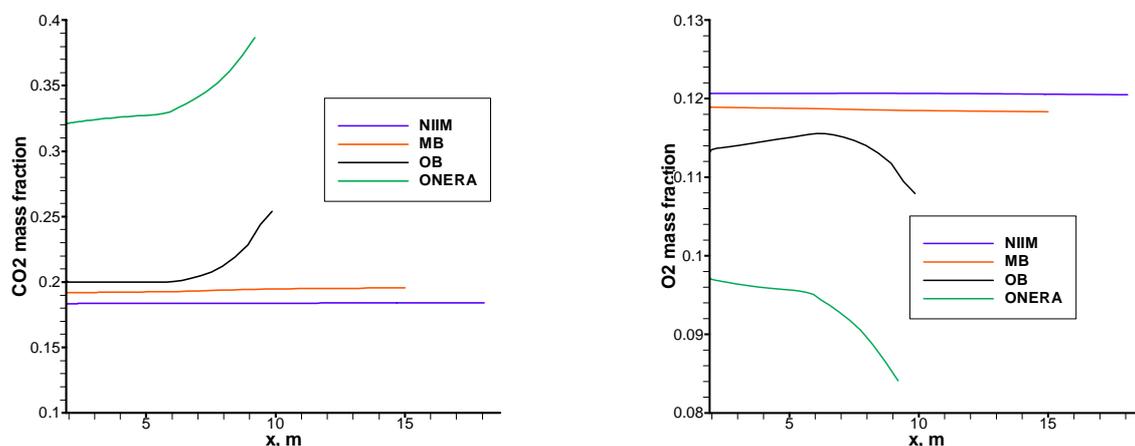Fig. 18: Pressure and temperature on the symmetry axes in the wake

Fig. 19: Mass fraction CO_2 & O_2 on the symmetry axis in the wake

The mass fractions of CO_2 & O_2 along the symmetry axis in the wake are illustrated in Fig. 19. NIIMech's calculations on the NIIMech, the G-MB-TC3-1 and the G-OB-TC3-1 grids are the closest. ONERA's CO_2 & O_2 mass fractions obtained on the G-OB-TC3-1 grid are different from NIIMech ones.

5.   RHT CONTRIBUTIONS

   The so-called mandatory case is based on the analysis of the radiative heat flux to select points of the body surface and in the wake. In this synthesis comparison will be made for radiative heat fluxes on the body surface versus distance along body surface from stagnation point.

   The comparison of the wall radiative heat fluxes on the front shield for NIIMech computations on all considered grids used are illustrated in Fig. 20.
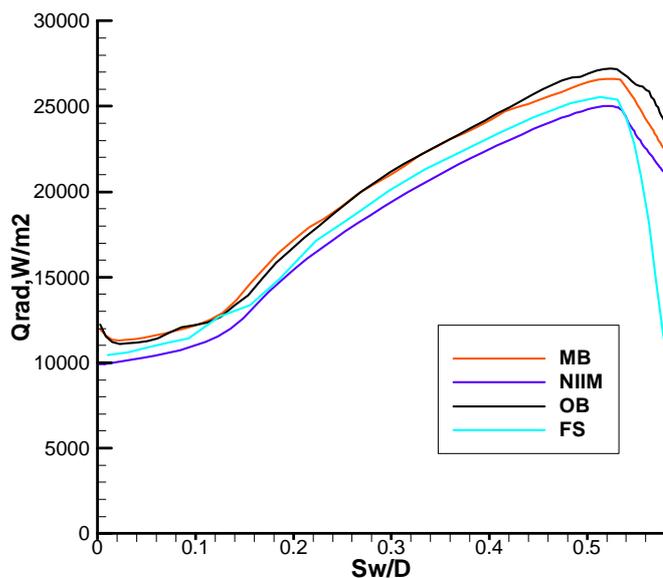
14

Fig. 20: Wall IR radiative heat flux on the front shield

Figure 21 shows comparison of the wall IR radiative heat flux predicted by NIIMech on the different grids and ONERA (without subtraction of the equilibrium wall radiation) for after-body surface. It is seen that radiative heat fluxes predicted on the back flat-end and shield using MB and NIIMech grids are higher than for another's. It could be explained by taking into account of radiation from more large regions for calculations on MB and NIIMech grids. Simultaneously, there is satisfactory agreement between wall after-body radiative heat fluxes predicted by NIIMech and in Ref. 2.
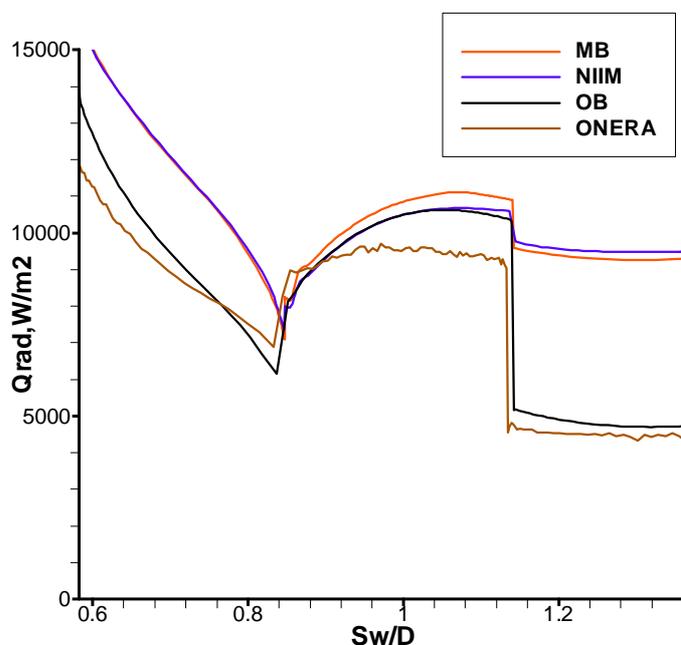

Fig. 21. Wall IR radiative heat flux on the after-body surface.

6.   CONCLUDING REMARKS

6.1 Flow solution on the front shield:
- shock adapted grid are provided a better capture of the flow,

- simultaneously, use shock adapted grid seems to be difficult for implementation in other codes,

- multi-block grids are advantageous for the whole flow field calculation,

- refinement along the wall should be required,

- simultaneously, unnecessary refinement to the wall should be discarded,

- comparing all contributions received, the variation heat flux on conical part of the shield is about 5%,

- simultaneously, the singularity phenomena in stagnation region prevents to exact conclusions

6.2. After-body flow solution:
- essential sensitivity of flow topology to the grid, scheme order and algorithm used,

- wall pressure and heat flux on the after-body is sensitive to circumstances mentioned above

- the grid has to allow the flow resolution around the corner of the cylinder-base

6.3. Radiative heat flux computations:
- large impact the spectral model used and gas flow on the radiative heat flux,

- comparison of the results on identical flow field is mandatory for radiative flow analysis

References

1. Workshop 2003 "Radiation of High Temperature Gas", TC3: Definition of an axially symmetric testcase for high temperature gas radiation prediction in Mars atmosphere entry, NG104-07-TF-001-CNES, 2003
2. Jean-Marc Charbonnier, Analysis of the results for TC3 presented at the 1st Int. Workshop on radiation on high temperature gas in planetary atmosphere entry, Proceeding of International Workshop on Radiation of High Temperature Gases in Atmospheric Entry, 8-10 October, Lisbon, Portugal, pp.145-159, 2003
3. Afonina N.E., Gromov V.G., Sakharov V.I., "HIGHTEMP Technique of High Temperature Gas Flow Numerical Simulation", Proc.of 5-th Europ. Symp. Aerothermodynamics for Space Applications, Nov.2004, Cologne, Germany
4. Surzhikov S.T., Computing System for Solving Radiative Gasdynamic Problems of Entry and Re-Entry Space Vehicles, Proc. RGD Workshop, 8-10, October, Lisbon, Portugal, 2003.
5. Hmelinin, B.A., Plastinin, Yu.A., "Emissivity and Absorptivity of H_2O, CO_2, CO and HCl molecules at temperatures 300-3000 K," Trudy TsAGI, No. 1656, 1975, pp.102-147 (in Russian)